A functional tool to explore the reliability of micro-earthquake focal mechanism solution for seismotectonic purposes

G.M.Guido Maria Adinolfi [1, 3,] *, R.Raffaella De Matteis [1], R.Rita de Nardis [2, 3] and A.Aldo Zollo [4]

[1] Dipartimento di Scienze e Tecnologie, Università degli Studi del Sannio ViaDe, via De Sanctis, 82100 Benevento, Italy

[2] Dipartimento di Scienze Psicologiche, della Salute e del Territorio, Università di Chieti-Pescara "G. d'Annunzio", vVia dei Vestini, 32, 66100, Chieti, Italy

[3] CRUST Centro inteRUniversitario per l'analisi SismoTettonica tridimensionale, Italy

[4] Dipartimento di Fisica, Università di Napoli "Federico II", Complesso Universitario di Monte S.Angelo, via Cinthia, 80124 Napoli, Italy

* Corresponding author: gmadinolfi@unisannio.it

ABSTRACT

Improving the knowledge of seismogenic faults requires the integration of geological, seismological, and geophysical information. Among several analyses, the definition of earthquake focal mechanisms plays an essential role in providing information about the geometry of individual faults and the stress regime acting in a region. Fault plane solutions can be retrieved by several techniques operating in specific magnitude ranges, both in the time and frequency domain and using different data.

For earthquakes of low magnitude, the limited number of available data and their uncertainties can compromise the stability of fault plane solutions. In this work, we propose a useful methodology to evaluate how well a seismic network, used to monitor natural and/or induced micro-seismicity, estimates focal mechanisms as a function of magnitude, location, and kinematics of seismic source and consequently their reliability in defining seismotectonic models. To study the consistency of focal mechanism solutions, we use a Bayesian approach that jointly inverts the P/S long-period spectral-level ratios and the P polarities to infer the fault-plane solutions. We applied this methodology, by computing synthetic data, to the local seismic network operating in the Campania-Lucania Apennines (Southern Italy) aimed to monitor the complex normal fault system activated during the Ms 6.9, 1980 earthquake. We demonstrate that the method we propose is effective and can be adapted for other case studies with a double purpose. It can be a valid tool to design or to test the performance of local seismic networks and more generally it can be used to assign an absolute uncertainty to focal mechanism solutions fundamental for seismotectonic studies.

40

INTRODUCTION

42

Fault plane solutions represent primary information ~~that seismologists can retrieve~~ to describe ~~the earthquake source~~earthquakes. The assessment of earthquake location, magnitude, and focal mechanism are the fundamental operations to characterize the earthquake source ~~through the~~using a point source approximation. ~~After the earthquake location, origin time, and source dimension are identified, the~~The focal mechanism describes the basic geometry and kinematics of a point source in terms of strike, dip, and rake of the fault plane along which the earthquake occurred. So, the focal mechanism is the most important ~~parameter that can be retrieved to recognize the~~ marker of the geometry of the seismogenic faults and their style of faulting. Moreover, ~~the~~ seismicity and focal mechanisms of events~~, also of small magnitudes,~~ are often used to constrain seismotectonic models, individual seismogenic sources, the regional strain, and stress fields~~.~~, also for small magnitudes. Consequently, an evaluation of their effective reliability becomes a fundamental issue in seismotectonic studies.

Nevertheless, focal mechanisms cannot be calculated and constrained every time an earthquake occurs. Although the calculation of focal mechanisms represents a routine analysis ~~inside the~~for seismological agencies, the solutions are calculated only for a specific range of magnitude~~s~~, usually greater than 4. In fact, constraining the solution for earthquakes with small magnitude is still ~~represents~~ a challenge, despite the advancement in the technological process and the use of increasingly performing seismic networks. This is due to several factors that we will analyse in detail. The techniques used to define the focal mechanism of large~~-~~ to moderate earthquakes are based on the inversion of the moment tensor, ~~that~~which corresponds to a stable and robust procedure, so much that it is the most common method for this type of analysis (Dreger, 2003; Delouis, 2014; Sokos and Zahradnik, 2013; Cesca et al., 2011). This technique requires accurate knowledge of the propagation medium in relation to the range of frequencies used for the modelling ~~of the~~ waveforms recorded during an earthquake. The smaller an earthquake, the higher the frequency range of the signal to be modelled, the more detailed the

knowledge and scale of the Earth's interior must be. Several methods have been proposed to achieve

a stable inversion of the moment tensor for earthquakes with a magnitude less than 3. Hybrid ~~approach~~

~~of the~~approaches that invert both amplitude and waveform moment tensor ~~inversions, which utilizes~~use

the principal component analysis of seismograms (Vavrycuk et al., 2017) or moment tensor refinement

techniques (Kwiatek et al. 2016; Bentz at al., 2018) to facilitate a robust determination of the source

type and its kinematics. In particular, the retrieved moment tensor is typically decomposed into

volumetric and deviatoric components. Constraining the earthquake as a double-couple source can

erroneously affect the retrieved fault plane solutions, especially in the case of induced seismicity where

the volumetric or non-double couple component must be considered (Kwiatek et al. 2016).

Other analytical techniques are based on the recognition of the source radiation pattern ~~that describes~~

~~the earthquake source.~~. According to the position of seismic stations ~~with respect~~relative to the source,

seismic waves on seismograms show different amplitudes and polarities. These features ~~are employed~~

~~in a very simple way by several algorithms to~~can constrain the geometry of the earthquake faulting

through estimating the angular parameters strike, dip, and rake. The classical method (Raesenberg and

Oppenheimer, 1985;) uses the P-wave polarities~~, but~~; more advanced ~~ones use~~approaches better

constrain the focal mechanism of small earthquakes using P- or S- wave amplitudes or amplitude ratios

together with first motions (Snoke, 2003~~) to better constrain the focal mechanism of small~~

~~earthquakes.~~). In fact, the use of polarities alone is ~~not convenient~~inappropriate, especially if we consider

micro-seismicity (M < 3). The reasons could be the limited number of available data, their uncertainties,

and the difficulty of measuring the P-polarity with a sufficient degree of precision. For these reasons,

different techniques using different types of measurements such as P-wave amplitudes (Julian and

Foulger, 1996; Tarantino et al., 2019), P/S or S/P amplitude ratios measured in the time or the

frequency domain (Kisslinger et al., 1981; Rau et al., 1996; Hardebeck and Shearer, 2003; De Matteis

et al., 2016), or S-wave polarizations (Zollo and Bernard, 1991) have been developed. The joint

inversion of polarities and amplitude ratios led to more stable and robust solutions, allowing to account

for geological site effects and to decrease ~~in first approximation~~ the effects produced by the geometric and anelastic attenuations.

Two kinds of errors generally influence the goodness of the solution and retrieved model (Michele et al., 2016): the perturbation errors that are related to how the uncertainty on data affects the model, and the resolution errors that are referred to the capability to retrieve a correct model, given a dataset as input or how accurate could be the model that we can recover, even ~~if~~with error-free data ~~are used~~. The sum of perturbation and resolution errors corresponds to the final errors on the model obtained by solving an inverse problem, as the solution of focal mechanism. In particular, the resolution errors depend on the available data, and so on the initial condition of the inverse problem. In the case of focal mechanism, the number of seismic stations, as well as the seismic network geometry, and the velocity structure of the crust influence the resolution and the reliability of the retrieved model.

How will the geometry of a seismic network determine the accuracy of focal mechanism solutions? The answer to this question ~~is not simple and~~ requires a deep knowledge of the geophysical and geological characteristics of the region, often ~~unrealistic~~unavailable. Moreover, the theoretical relationships that predict the focal mechanism solutions for an earthquake scenario could be very complicated if several factors, such as network configuration, noise level, source magnitude, or source kinematics are taken into account. ~~We want to underline that a~~A network configuration may be optimal for earthquake locations, but not for retrieving fault plane solutions (Hardt and Scherbaum, 1994). In fact, a given geometry may resolve some fault kinematics better than others.

A seismic network layout is strictly associated with the goals of the network and the available funds; according to these features, a network operator decides how many stations are required and where they should be located (Havskov et al.; 2011). So, the number of seismic stations, the size, and geometry of the network are defined after a preliminary phase based on the evaluation of the specific seismological target (Trnkoczy et al., 2009; Hardt and Scherbaum 1994; Steinberg et al. 1995; Bartal et al. 2000). In the case of small earthquakes, the available recordings come from only a portion of the total network, while the distant stations show a seismic signal buried inside the noise. In order to detect

118 and locate low-magnitude earthquakes, we must increase the number of seismic stations for area units

119 by building a dense seismic network.

120 In this study, we propose a useful tool to evaluate both 1) the reliability of focal mechanism solutions

121 inferred by the inversion of different seismological data and 2) the performance of the seismic network

122 to assess focal mechanism solutions and their errors. We evaluate the network capability to solve focal

123 mechanisms as a function of magnitude, location, and kinematics of seismic source. We consider three

124 synthetic data set: P-wave polarities, P- S-wave amplitude spectral ratios and polarities and amplitude

125 ratios together. Moreover, different levels of noise are considered in order to simulate more realistic

126 conditions.

127 We selected as target the Irpinia Seismic Network (ISNet), a local seismic network that monitors the

128 Irpinia complex normal fault system (Southern Italy), activated during the Ms 6.9 earthquake of 23rd

129 November 1980. Evaluating the specific performance of an existing network for a seismological goal is

130 critical and can be used to decide how to improve its layout.

131

132 **METHODOLOGY**

133 With the main aim to define the reliability of focal mechanisms retrieved by specific seismic networks,

134 we propose a methodology based on an empirical approach that consists of different steps.

135 *Configuration and Parameter Tuning (Step 1).* In a preliminary phase, we select for each earthquake

136 simulation the: a) fault plane solution to test, b) seismic observables to be computed (i.e. P-wave

137 polarities or P- S-wave amplitude spectral ratios), c) magnitude, d) the earthquake epicentre and depth;

138 e) the network geometry; f) the noise level. The fault plane solution to test can be derived from

139 instrumental seismicity as one of the strongest earthquakes occurred in the area or a median solution

140 of the available ones or simply a fault plane solution representative of the regional seismotectonic.

141 Once the network geometry and the hypocentre of the earthquake are defined, the seismic stations

142 (number and type) for which the synthetic data are computed must be selected. The number of seismic

143 stations that record an event depends on earthquake magnitude, source-stations distance, crustal

144 medium properties, and the level of noise. We use an empirical approach, based on the statistical

145 analysis of the local seismicity catalog, that allows us to define, for each magnitude range, a maximum

146 (threshold) epicentral distance for which only the seismic stations within this distance are considered

147 (See data analysis).

148 *Synthetic Data Computation (Step 2)*. Using a crustal velocity model and the source-receiver relative

149 position, the synthetic data are computed for the theoretical fault plane solution. The seismic

150 observables that can be reproduced are a) P-wave polarities, b) P/S spectral amplitude ratios, and c)

151 polarities and amplitude ratios together. For the P/S spectral level ratios, the Gaussian noise level is

152 added.

153 *Focal Mechansim Inversion (Step 3).* We estimated focal mechanism using BISTROP code (De Matteis

154 et al., 2016) that jointly inverts the ratio between the P- and S-wave long-period spectral levels and

155 the P-wave polarities according to a Bayesian approach. BISTROP has the advantage to use different

156 observables for the determination of fault plane solutions, such as the P/S long-period spectral level

157 ratios or P-wave polarities, individually or together. The benefits of the use of spectral level ratios are

158 multiples: 1) they can be measured for a broad range of magnitudes (also for M < 3; De Matteis et al.,

159 2016); 2) they can be calculated by automatic procedures without visual inspection; 3) their estimates

160 do not require to identify the first arrival time accurately, but only a time window of signal containing

161 P- or S-phase is mandatory and 4) the spectral amplitude ratios, they can generally be used without

162 the exact knowledge of the geological soil conditions (site effects) and geometric/anelastic attenuation.

163 Moreover, the joint inversion of amplitude spectral ratios and polarities led to constraining fault plane

164 solutions reducing the error associated with the estimates of retrieved parameters. BISTROP solves an

165 inverse problem through a probabilistic formulation leading to a complete representation of uncertainty

166 and correlation of the inferred parameters.

167 For a double-couple seismic source, the radiation pattern depends on fault kinematics and relative

168 source-station position. In fact, it can be represented as a function of 1) strike, dip and rake angles (φ,

169 δ, λ) and 2) take-off and azimuth angles (i_h, φ_r). We can define the ratio between P- and S-wave

170 radiation pattern coefficients as:

171
$$\frac{\mathcal{R}^P\left(\phi,\delta,\lambda,i_h,\phi_R\right)}{\mathcal{R}^S\left(\phi,\delta,\lambda,i_h,\phi_R\right)} = \left(\frac{\alpha_s^2\alpha_r}{\beta_s^2\beta_r}\right)\ \frac{\Omega_0^P}{\Omega_0^S} \qquad (1)$$

172 where Ω_0^P and Ω_0^S are the long-period spectral level of the P- and S-waves, respectively, and α_s, α_r,

173 β_s, β_r, are the P- and S-wave velocities at the source and at the receiver, respectively. Thus, using the

174 displacement spectra, assuming a given source and attenuation model (Boatwright, 1980), we can derive

175 from the signal recorded by a seismic station the ratio of radiation pattern coefficients for P- and S-

176 phases, as well as α, β, i_h, φ_r are known from the earthquake location and the velocity model used. So,

177 from a theoretical point of view, the spectral amplitude ratios measured at several seismic stations can

178 be used to retrieve the ratio of radiation pattern coefficients $\mathcal{R}_{\theta\varphi}^P/\mathcal{R}_{\theta\varphi}^S$ as a function of the source-

179 receiver azimuth and take-off angles.

180 BISTROP jointly inverts the spectral amplitude ratios with the observed P-wave polarities to infer the

181 parameters φ, δ, λ of the focal mechanism in a Bayesian framework. A posterior probability density

182 function (PDF), for the vector of model parameter $\boldsymbol{m}$ (φ, δ, λ) and the vector of observed data $\boldsymbol{d}$, is

183 defined as:

184
$$q(\boldsymbol{m}|\boldsymbol{d}) = \frac{f(\boldsymbol{d}|\boldsymbol{m})p(\boldsymbol{m})}{\int_M f(\boldsymbol{d}|\boldsymbol{m}')p(\boldsymbol{m}')\,d\boldsymbol{m}'} \qquad (2)$$

185

186 where $f(\mathbf{d}|\mathbf{m})$ is the conditional probability function that represents the PDF given the data $\mathbf{d}$ and for

187 parameter vector $\boldsymbol{m}$ in the model parameter space $\boldsymbol{M}$, and $p(\boldsymbol{m})$ is the a priori PDF. If P-wave polarities

188 and P/S spectral level ratios are independent datasets, the conditional probability function may be

189 written as:

190

191
$$f(\mathbf{d}|\mathbf{m}) = f(\boldsymbol{d}^L|\mathbf{m})f(\boldsymbol{d}^P|\mathbf{m}). \qquad (3)$$

192

193   in which the pdf of the data vector $\boldsymbol{d}^L$ of N^L measurements of spectral ratios is multiplied for the pdf

194   of data vector $\boldsymbol{d}^P$ of N^P measurements of P-wave polarities given the model $\boldsymbol{m}$.

195   Assuming that the observables have the same finite variance, for the N^L observations of spectral level

196   ratios the conditional probability function may be defined as:

197
$$f(\boldsymbol{d}^L|\boldsymbol{m}) = \frac{1}{\left(\sqrt{2\pi}\sigma\ \right)^{N_L}} exp\left(-\frac{\sum_{i=1}^{N_L}\{d_i - [G(\boldsymbol{m})]_i\}^2}{2\sigma^2}\right) \qquad (4)$$

198

199   Where $G(\boldsymbol{m})$ represents a functional relationship between model and data and corresponds to Equation

200   1 and σ represents the uncertainty on the spectral measure.

201   For the N^P observations of P-wave polarities, the conditional probability function is (Brillinger et al.,

202   1980):

203
$$f(\boldsymbol{d}^P|\boldsymbol{m}) = \prod_{i=1}^{N_P} \frac{1}{2}[1 + \psi(\mathcal{R}_i^P, \gamma_i, \rho_0)Y_i sign(\mathcal{R}_i^P)] \qquad (5)$$

204

205   in which:

206   .

207
$$\psi(\mathcal{R}_i^P, \gamma_i, \rho_0) = (1 - 2\gamma_i)\,\text{erf}\big(|\rho_0\mathcal{R}_i^P(\boldsymbol{m})|\big) \qquad (6)$$

208

209   The quantity reported in square brackets in Equation 5 represents the probability that the observed i_{th}

210   polarity γ_i is consistent with the theoretical one computed from the model $\boldsymbol{m}$, whose theoretical P-wave

amplitude is $\mathcal{R}_i^P$ and $sign(\mathcal{R}_i^P)$ is its polarity at i_{th} station for a given fault plane solution. The

parameters ρ_s and γ_0 , referring to the errors in ray tracing due to velocity model ambiguity and to the

uncertainty on polarity reading, regulating the shape of the PDF. For more details about the

mathematical formulation, see De Matteis et al. (2016).

Evaluation of the Results (Step 4).   Once the best solution is estimated, the focal mechanism

uncertainties and its misfit, respect to the theoretical solution as Kagan angle, are computed. The focal

mechanism parameter (strike, dip and rake) misfit and their uncertainties are also calculated.

IRPINIA SEISMIC NETWORK

As testing case of our methodology, we choose the area of the M 6.9, 1980 Irpinia earthquake

(Southern Italy). Since 2005, ISNet, a local, dense seismic network monitors the seismicity along the

Campania-Lucania Apennines covering an area of about 100 × 70 km^2 (Figure 1; Weber et al., 2007).

The seismic stations are deployed within an elliptic area whose major axis, parallel to the Apennine

chain, has a NW-SE trend with an average inter-stations distance of 15 km that reaches 10 km in the

inner central zone. Each seismic station ensures a high dynamic range and it is equipped with a strong-

motion accelerometer, Guralp CMG-5T or Kinemetrics Episensor, and a short period three-component

seismometer, Geotech S13-J with a natural period of 1 sec. In 6 cases, broadband seismometers are

installed such as the Nanometrics Trillium with a flat response in the range 0.025–50 Hz. ISNet is

operating by INFO (Irpinia Near Fault Observatory) and it provides real-time data at local control centres

for earthquake early warning systems or real-time seismic monitoring (Satriano et al., 2011). Seismic

events are automatically identified and located from continuous recordings by automatic Earth-worm

Binder and data are then manually revised by operators (Festa et al., 2020).

The 1980, M 6.9, Irpinia earthquake was one of the most destructive, instrumental earthquakes of the

Southern Apennines, causing about 3000 fatalities and severe damages in the Campania and Basilicata

regions. It activated a NW-SE trending normal fault system with a complex rupture process involving

236 multiple fault segments according to (at least) three different nucleation episodes delayed each other

237 of 20 s (Bernard and Zollo, 1989; Pantosti and Valensise; 1993; Amoruso et al.; 2005). No large

238 earthquakes occurred in the Irpinia region since 1980. A Mw 4.9 earthquake took place in 1996

239 originating a seismic sequence inside the epicentral area of the 1980 earthquake (Figure 1; Cocco et

240 al., 1999). Recent instrumental seismicity occurs mainly in the first 15 km of the crust showing fault

241 plane solutions with normal and normal-strike slip kinematics, indicating a dominant SW-NE extensional

242 regime (Pasquale et al., 2009; De Matteis et al., 2012; Bello et al., 2021). Low-magnitude seismicity

243 (M_L < 3.6) is spread into a large volume related to the activity of major fault segments of the 1980

244 Irpinia earthquake (Figure 1; Adinolfi et al., 2019; Adinolfi et al., 2020). Seismic sequences or swarms

245 often occurred in the area, extremely clustered in time (from several hours to a few days) and space

246 and seem to be controlled by high pore fluid pressure of saturated Apulian carbonates bounded by

247 normal seismogenic faults (Stabile et al., 2012; Amoroso et al, 2014).

248

DATA ANALYSIS

250 We applied the method we proposed and evaluated the capability of the ISNet local network to resolve

251 fault plane solutions using different observables as input data: a) P-wave polarities, b) P/S spectral

252 amplitude ratios and c) polarities and amplitude ratios together. the analysis is carried out by evaluating

253 the effect of 1) earthquake magnitude, 2) epicentral location, 3) earthquake depth, 4) signal-to-noise

254 ratio, and 5) fault kinematics on retrieved focal solutions as previously described.

255 *Step 1*. In order to selectfocal mechanisms (FMs) to be used for our resolution study (Figure 2a), we

256 carried out statistical analysis to define the most frequent fault plane solutions of instrumental

257 seismicity. We classified, according to the plunge of P- and T-axes, the fault plane solutions reported

258 in De Matteis et al. (2012) choosing only the FMs occurring within the Irpinia area since 2005 to 2011.

259 As shown in Figure 2b, splitting the range of the data into equal-sized bins, we selected the focal

260 mechanism corresponding to the median value of the most populated class. We report it in Figure 2a

261   as FM2. This corresponds to a normal-strike-slip fault plane solution with strike, dip, and rake equal to

262   292°, 53°, and -133°, respectively. Then, we decided to test the focal mechanism solution of the1980

263   Irpinia earthquake, a pure normal fault (strike, dip, rake: 317°, 59°, -85°; Westaway and Jackson, 1987;

264   Fig. 2a) here and after FM1. This solution is very similar to the focal mechanism corresponding to: 1)

265   the regional stress field (see Supplementary Material); 2) the M_L 2.9, Laviano earthquake, one of the

266   most energetic earthquakes of the last years (Stabile et al.; 2012), and 3) those of the 2nd, 3rd, 4th most

267   populated bins. Finally, we selected the solution corresponding to the 5th bin reported as FM3 in Figure

268   2a. This focal mechanism is quite different from the others due to a predominant component along the

269   fault strike (strike, dip, rake: 274°, 71°, -128°)

270   *Step 2.* For each of the three selected fault plane kinematics, we calculated synthetic data (P-wave

271   polarities or P- and S-wave spectral amplitudes) at seismic stations varying the earthquake location and

272   by using a local velocity model (Matrullo et al., 2013). We discretize the study area with a square grid

273   (100 X 100 km^2), centred on the barycentre of ISNet, with 441 nodes and a sampling step of 5 km.

274   Each node corresponds to a possible earthquake epicentre (Figure 3).

275   For each grid node and according to the earthquake magnitude to be tested, we have to select the

276   ISNet stations for simulations. The number of seismic stations that record an event depends on

277   earthquake magnitude, source-stations distance, crustal medium properties, and the noise level.

278   Theoretical relationships that link the seismic source to the signal recorded at every single station are

279   quite complicated (Kwiatek et al., 2016; 2020) and are based on the accurate knowledge of crustal

280   volumes in which the seismic waves propagated, such as the three-dimensional wave velocity structure,

281   anelastic attenuation or/and site conditions of a single receiver. To overcome this limitation, we used

282   an empirical approach to define the number and the distance of the seismic stations that record a

283   seismic signal as a function of magnitude, once its epicentral location (grid node) and depth are fixed.

284   Using the bulletin data retrieved by INFO at ISNet during the last two years (January 2019-March 2021;

285   http://isnet-bulletin.fisica.unina.it/cgi-bin/isnet-events/isnet.cgi), we selected two earthquake catalog

286   datasets with depths equal to 5 (+- 2) km and 10 (+- 2) km, respectively, and local magnitude ranging

between 1.0 and 2.5. These choices are motivated by the characteristics of the Irpinia micro-seismicity recorded by ISNet. Then, we divided each dataset into bins of 0.5 magnitudes and for each bin, we retrieved the median number of P-wave polarity readings and the median epicentral distance of the farthest station that recorded the earthquake (Table 1). The bulletin data are manually revised by operators, and we selected only seismic records that provide P- and/or S- wave arrival times. The median value of the distance of the farthest station is then used to select the seismic stations for which synthetic data are calculated. Therefore, for each earthquake simulation of specific magnitude and depth, only the seismic stations with a distance, from the grid node under examination (epicentre), equal or lower than the maximum distance, reported in Table 1, are considered. We run simulations only for earthquakes recorded at least by 6 seismic stations. The synthetic P-wave polarities are simulated only at a number of stations corresponding to the median value previously defined. (Table 1). We pointed out that the number of P-wave polarities empirically assigned is related to the available earthquake catalogue data of the Irpinia region where the seismicity can occur in different portions of the area covered by the network, not always with optimal azimuthal coverage.

Additionally, we simulated the uncertainty on the measure of spectral level ratios or the effect of seismic noise adding a zero mean, Gaussian noise to the synthetic data with a standard deviation equal to two different percentage levels, as 5% and 30%. With this configuration, we simulated:

- Three datasets of seismic observables: P-wave polarities (D1), P/S spectral level ratios (D2) and polarities and P/S spectral level ratios together (D3)

- Two hypocentre depths: 5 km and 10 km

- Three magnitude bins: M_L 1.0 -1.5 (M1), M_L 1.5 - 2.0 (M2) and M_L 2.0 - 2.5 (M3)

- Three focal mechanism solutions: FM1 (317°, 59°, -85°), FM2 (292°, 53°, -133°) and FM3 (274°, 71°, -128°)

Two level of Gaussian noise: 5% and 30%. When D2 is simulated, in order to solve the verse ambiguity of the slip vector, a P-wave polarity is added to the earthquake data to be inverted for the focal mechanism.

313 *Step 3*. For each earthquake simulation the focal mechanism was estimated by inverting the synthetic

314 data with BISTROP (De Matteis et al.; 2016).

315 *Step 4*. In order to analyse the results, we defined five kinds of map to study how the focal mechanism

316 (FM) resolution and error spatially change in the area where ISNet is installed (Table 2):

317

318 • Kagan angle misfit map (KAM)

319 • Map of the focal mechanism parameter misfit (FMM)

320 • Strike, Dip and Rake error map (FME)

321 • Kagan angle average map (KAA)

322 • Kagan angle standard deviation map (KAS)

323

324 The Kagan Angle (KA) measures the difference between the orientations of two seismic moment tensors

325 or two double couples. It is the smallest angle needed to rotate the principal axes of one moment tensor

326 to the corresponding principal axes of the other (Kagan et al.; 1991; Tape and Tape; 2012). The smaller

327 the KA between two focal mechanisms, more similar they are. In KAM map, for each node the value of

328 KA between the theoretical and retrieved solution is reported, while in FMM map, the absolute value of

329 the misfit between the strike, dip, and rake angles of the retrieved and theoretical solution is indicated.

330 FME is defined as the error map of strike, dip, and rake in which the uncertainties (standard deviations)

331 are calculated considering all the solutions with probability larger than the 90% (S90) of the maximum

332 probability, corresponding to the best solution retrieved. Additionally, these solutions are used to study

333 how constrained is the FM solution. The KA is calculated between each FM of S90 solutions and the

334 retrieved best solution. The mean and the standard deviation of the resulting KA distribution are plotted

335 in KAA and KAS maps, respectively. The smaller KA mean and std, the more constrained is the obtained

336 fault plane solution (Table 2).

337

338 **DISCUSSION**

We consider the FM1, i.e. the focal mechanism of the 1980 Irpinia earthquake located at 10 km depth,
first. Looking at Figures 4 and 5, we see the effect of using the three different datasets. Considering
D1, we can calculate the FM only for earthquakes with magnitude 2.0-2.5 for which at least 6 polarities
are available. As shown by KAM map in Figure 4a, the retrieved solutions are characterized by high KA
(> 50°) with limited areas or single nodes with values in the range 40°-50°. Therefore, D1 ~~is not~~
~~sufficient to~~cannot retrieve with acceptable accuracy the FMs for earthquakes with magnitude 2.0-2.5.
The same result is obtained for FM2 and FM3 (Figure 4b-c). Comparing the results of the simulations
using D2 and D3 (Figure 5), the accuracy of the retrieved solution is improved when P-wave polarities
data are added to spectral level ratios. The areas in KAM map with high value of KA (KA $\geq$ 18°; red or
green areas) disappear or are strongly reduced. Nevertheless, ~~we want to underline that,~~ even with D2
dataset, ~~exception some small areas,~~ the FMs are well retrieved for all magnitudes with the KA misfit
mostly lesser than 10~~°.~~°, except in some small areas. The spatial resolution of the network is strongly
influenced by the earthquake magnitude. In fact, for both M1 and M2, there are nodes (white areas
where we assume the KA = -1 as an indeterminate value) for which the FMs cannot be calculated
because ~~a~~less than 6 stations (the minimum number ~~of stations (at least 6~~) are ~~not~~ available (Table 1).
At the same time, the areas better resolved correspond to the region inside the network~~, although with.~~
With D2 and D3 acceptable solutions are calculated for M1 and M2 earthquakes also outside the
network, (Figure 5).

Looking at Figure 6, using the D3 dataset, ~~we observe that, among the FM parameters,~~ the dip angle
is the best resolved compared with strike and rake angles. ~~Considering~~For the M2 and M3 focal
mechanisms, the misfit of dip is very low (< 8°), followed, in ascending order, by rake and strike that
show higher values (10° < misfit < 22°). For M1 (Figure 6a-d-g), rake and strike misfits are larger than
50°, with rake worse resolved than strike. The unresolved areas correspond to the regions outside the
seismic network.

The KAA and KAS maps (Figures 7 and 8) show how the network constrains the fault plane solution as
a function of the epicentral location. Moreover, Figures 7d-e-f and 8d-e-f indicate that the areas with
KA mean and ~~std~~standard deviation greater than 30° and 20°, respectively, are reduced when P-wave

polarities and spectral level ratios data are used. On ~~the~~ contrary, only for M1 focal mechanisms, there is no improvement because the number of P-wave polarities is the same for both D2 and D3 datasets (Table 1). The worst constrained regions correspond to a belt surrounding the seismic network, with KA mean < 30° and KA std < 20° for M2 and M3 solutions. For M1, areas with high uncertainty remain outside and inside the network, specifically in the central and eastern sectors.

Looking at the uncertainties of FM parameters, obtained by using the D3 dataset, Figure 9 shows that the dip is the better-constrained parameter with an error < 10°, also for M1 solutions. The rake angle shows an uncertainty l~~ow~~esser than 20° for M2 and M3, while it ~~overcomes~~higher than 50° for M1. The strike angle ~~reveals~~has the highest uncertainty, with values greater than 50° in the eastern and southern sectors of the map for ~~all~~any analysed magnitudes (M1, M2, and M3). Accuracy improves moving from M1 to M3 earthquakes.

~~As shown in Figure 10, the~~The accuracy of fault plane solutions~~, in terms of KA misfit calculated by~~ evaluated using the KA misfit and D3 dataset~~,~~ is similar for FM1, FM2, and FM3, mostly with values lesser than 8° for all the magnitudes ~~M1, M2, and M3.~~(Figure 10). FM2 and FM3 show a slightly higher precision than FM1 in the area inside the seismic network (see FMM, FME, KAA, and KAS maps for FM2 and FM3 in Supplementary Material). In the regions outside the network, where the azimuthal gap increases, the FMs better constrained in descending order are: FM3, FM2, and FM1. This effect should be due to the geometric relationship between the spatial distribution of the seismic stations and the orientation of the principal axes (P, T, B) that characterize the FMs.

Considering the effect of hypocentre depth, the results achieved for earthquakes at 5 km depth, by using the D3 dataset, are overall unchanged (Figure 11). We note that the fault plane solutions are slightly worse resolved due to a smaller number of P-wave polarities available for M2 and M3. The KA misfit ~~mainly~~generally is lesse~~r~~ than 10°, even though the number and the dimension of areas with misfits> 20° are greater than those obtained considering earthquakes at 10 km depth. Moreover, the dip angle shows a misfit lower than strike and rake angles for M1, M2, and M3; the accuracy of the retrieved FMs parameters is mainly lesse~~r~~ than 8°, as shown in Figure 11.

Previous analyses are carried out considering ~~by using~~ data affected by 5% Gaussian error. In the last test, we simulated synthetic data adding a 30% Gaussian error. As illustrated in Figure 12, FM solutions show an overall larger misfit, in particular, the KA inside the seismic network is less than 20°. The area best resolved (KA < 8°) is ~~considerably~~ reduced to ~~a small~~the central portion of the network. This result indicates that the accuracy of the spectral level ratio estimates is crucial: noisy waveforms with a low signal-to-noise ratio can critically affect the result of the focal mechanism inversion. So, seismic noise as well as the number of available stations, variable due to the operational condition~~s~~, strongly influence the capability of the seismic network to retrieve a fault plane solution. Using the results of our simulations, we classified the focal mechanism provided by De Matteis et al. (2016) according to a quality code based on the resolution of fault kinematics (Table 3). In fact, we assigned to focal mechanisms of the Irpinia instrumental seismicity a quality~~ies~~ A, B and C for the solutions that fall into the bins relative to FM3, FM2 and FM1 kinematics, respectively. The quality A, B and C correspond to the average value of KA misfit (FM3=2.4°, FM2=3.1°, FM1=4.5°) calculated for M1, M2 and M3 magnitudes using D3 dataset and considering earthquakes at 10 km depth with 5% Gaussian errors. As last analysis, we carried out a test in a more general framework, without a fixed network configuration. We explored the reliability of focal mechanism estimation as a function of the uniformity of the focal sphere coverage, defined by the number of recording seismic stations and azimuthal gap. We simulated 10400 earthquakes fixing the fault plane solution and varying: 1) the number of seismic stations (6-30), 2) the take-off angle and 3) the azimuth of each single station. For each possible number of seismic stations, we run about 400 simulations, and we randomly sampled the focal sphere varying the azimuth and take-off of the stations ~~and, so,~~, thus changing the geometrical configuration of our virtual network of each simulation. We computed the KA between the theoretical and retrieved focal mechanism (best) solutions~~,~~ using only P-polarities~~,~~ for each simulation. We show the results in ~~the~~ Figures 13 and S7, as 3-D histograms and 3-D scatter plot, respectively. In ~~the~~ Figures 13a, as expected, ~~we note that, as~~ the number of stations increases,while the KA and its range of variation decrease. If the number of stations is less than nine, only few solutions have KA<40°. Figure 13b shows that ~~the~~ most value of KA less than 30° are obtained for azimuthal gap less than about 80°. ~~Moreover,~~

these evidences are shown in theIn Figure S7, where the relation among the KA, azimuthal gap and number of stations is clearified by the three-dimensional spatial point patterns as well by the projections of the data on the three coordinate planes.

CONCLUSIONS

We studied the focal mechanism reliability retrieved by the inversion of data recorded by ISNet, a local dense seismic network that monitors the Irpinia Fault System in Southern Italy. Three different datasets of seismological observables are used as input data for focal mechanism determination: a) P-wave polarities, b) P/S long-period spectral amplitude ratios, and c) joint polarities and amplitude ratios. Starting from empirical observations, we computed synthetic data for a regular grid of epicentre locations at two depths (5 and 10 km), for earthquake magnitude in the range 1.0-2.5, and for three focal mechanism solutions. Two different levels of   Gaussian error (5% and 30%) are added to the data.

Main conclusions can be summarized as follows.Our results show that:

- The joint inversion of P-wave polarities and P/S spectral amplitude ratios allows retrieving accurate FM (KA misfit < 8°) also for earthquakes with magnitude ranging between 1.0 and 2.5, at depths of 5 km and 10 km. Due to the low-energy magnitude, the number of P-wave polarities is not adequate tocannot constrain fault plane solutions.

- The spatial resolution analysis of ISNet shows that the most accurate FM solutions are obtained for earthquakes located inside the network with —strike, dip and rake misfit < 8°. Nevertheless, outside the network or at its borders, acceptable solutions can be calculated even if the azimuthal coverage is not adequateinaadequate (especially for M2 and M3 events). This peculiarity is due to the geometrical relationship between the recording seismic stations and the orientation of the principal axes (P, T, B).

- The geometry of the network allows to well resolve well fault plane solutions varying between normal and normal-strike focal mechanism with mainly strike, dip and rake misfit lessergenerally

less than 10° and for the magnitude range 1.5-2.5. The network resolves ~~a~~ slightly better normal-strike fault plane solution than ~~a~~ pure normal focal mechanism.

- Among the FM parameters, the dip angle shows the lowest uncertainty. Strike and rake angles ~~reveal~~have higher errors especially for M 1-1.5 earthquakes in the region outside the seismic network.

- ~~Dataset affected by~~ Adding a 30% Gaussian error ~~provide a worsening in~~worsens the accuracy of the retrieved FMs. ~~Although~~Despite the ~~high error level, the area of well resolved~~higher uncertainty, fault plane solutions (KA misfit < 20°) ~~persists~~are still resolved in the central part of the network, especially for M2 and M3.

The methodology described in this work can be a valid tool to design ~~or to~~and test the performance of local seismic networks, aimed at monitoring natural or induced seismicity. Moreover, given a network configuration, it can be used to evaluate the reliability of FMs or to classify ~~the retrieved~~ fault plane solutions that represent a fundamental information in seismotectonic studies. Although it is a theoretical study, many earthquake scenarios with several magnitude, locations and noise conditions can be simulated to mimic the real seismicity.

REFERENCES

Adinolfi, G. M., Cesca, S., Picozzi, M., Heimann, S., & Zollo, A. (2019). Detection of weak seismic sequences based on arrival time coherence and empiric network detectability: an application at a near fault observatory. *Geophysical Journal International*, *218*(3), 2054-2065.

Adinolfi, G. M., Picozzi, M., Cesca, S., Heimann, S., & Zollo, A. (2020). An application of coherence-based method for earthquake detection and microseismic monitoring (Irpinia fault system, Southern Italy). *Journal of Seismology*, *24*, 979-989.

Amoroso, O., Ascione, A., Mazzoli, S., Virieux, J., & Zollo, A. (2014). Seismic imaging of a fluid storage in the actively extending Apennine mountain belt, southern Italy. *Geophysical Research Letters*, *41*(11), 3802-3809.

Amoruso, A., Crescentini, L., & Scarpa, R. (2005). Faulting geometry for the complex 1980 Campania-Lucania earthquake from levelling data. *Geophysical Journal International*, *162*(1), 156-168.

Bartal, Y., Somer, Z., Leonard, G., Steinberg, D. M., & Horin, Y. B. (2000). Optimal seismic networks in Israel in the context of the Comprehensive Test Ban Treaty. *Bulletin of the seismological society of America*, *90*(1), 151-165.

Bello, S., De Nardis, R., Scarpa, R., Brozzetti, F., Cirillo, D., Ferrarini, F., ... & Lavecchia, G. (2021). Fault Pattern and Seismotectonic Style of the Campania–Lucania 1980 Earthquake (M w 6.9, Southern Italy): New Multidisciplinary Constraints. Front. *Earth Sci*, *8*, 608063.

Ben-Menahem, A., and S. J. Singh (1981). Seismic Waves and Sources, 1108 p, Springer-Verlag, New York.

Bentz, Stephan, P. Martínez-Garzón, G. Kwiatek, M. Bohnhoff, and J. Renner (2018). Sensitivity of Full Moment Tensors to Data Preprocessing and Inversion Parameters: A Case Study from the Salton Sea Geothermal Field. Bull. Seismol. Soc. Am. 108, 588–603, doi 10.1785/0120170203

Bernard, P., & Zollo, A. (1989). The Irpinia (Italy) 1980 earthquake: detailed analysis of a complex normal faulting. *Journal of Geophysical Research: Solid Earth*, *94*(B2), 1631-1647.

Boatwright, J. (1980). A spectral theory for circular seismic sources; simple estimates of source dimension, dynamic stress drop, and radiated seismic energy, *Bull. Seismol. Soc. Am.*, **70** (7), 1–27.

Brillinger, D. R., A. Udías, and B. A. Bolt (1980). A probability model for regional focal mechanism solutions, *Bull. Seism. Soc. Am.* **70**, 149- 170.

Cesca, S., Heimann, S., Stammler, K., & Dahm, T. (2010). Automated procedure for point and kinematic source inversion at regional distances. *Journal of Geophysical Research: Solid Earth*, *115*(B6).

Cocco, M., Chiarabba, C., Di Bona, M., Selvaggi, G., Margheriti, L., Frepoli, A., ... & Campillo, M. (1999). The April 1996 Irpinia seismic sequence: evidence for fault interaction. *Journal of Seismology*, *3*(1), 105-117.

Delouis, B. (2014). FMNEAR: Determination of focal mechanism and first estimate of rupture directivity using near-source records and a linear distribution of point sources. *Bulletin of the Seismological Society of America*, *104*(3), 1479-1500.

De Matteis, R., Matrullo, E., Rivera, L., Stabile, T. A., Pasquale, G., & Zollo, A. (2012). Fault delineation and regional stress direction from the analysis of background microseismicity in the southern Apennines, Italy. *Bulletin of the Seismological Society of America*, *102*(4), 1899-1907.

De Matteis, R., Convertito, V., & Zollo, A. (2016). BISTROP: Bayesian inversion of spectral-level ratios and P-wave polarities for focal mechanism determination. *Seismological Research Letters*, *87*(4), 944-954.

Dreger, D. S., Lee, W. H. K., Kanamori, H., Jennings, P. C., & Kisslinger, C. (2003). Time-domain moment tensor INVerse codel (TDMT-INVC) release 1.1. *International Handbook of Earthquake and Engineering Seismology, WHK Lee, H. Kanamori, PC Jennings, and C. Kisslinger (Editors), Vol. B*, 1627.

Festa, G., Adinolfi, G. M., Caruso, A., Colombelli, S., De Landro, G., Elia, L., ... & Zollo, A. (2021). Insights into Mechanical Properties of the 1980 Irpinia Fault System from the Analysis of a Seismic Sequence. *Geosciences*, *11*(1), 28.

Hardebeck, J., and M. Shearer (2003). Using S/P Amplitude Ratios to Constrain the Focal Mechanisms of Small Earthquakes, *Bull. Seism. Soc. Am.* **93**, 6, pp. 2434–2444, December 2003.

Hardt, M., & Scherbaum, F. (1994). The design of optimum networks for aftershock recordings. *Geophysical Journal International*, *117*(3), 716-726.

Havskov, J., Ottemöller, L., Trnkoczy, A., Bormann, P. (2012): Seismic Networks. - In: Bormann, P. (Ed.), *New Manual of Seismological Observatory Practice 2 (NMSOP-2)*, Potsdam : Deutsches GeoForschungsZentrum GFZ, 1-65.

Julian, B. R., and G. R. Foulger (1996). Earthquake mechanisms from linear-programming inversion of seismic-wave amplitude ratios, *Bull. Seism. Soc. Am.* **86** (4), 972-980.

Kagan, Y. Y. (1991). 3-D rotation of double-couple earthquake sources. *Geophysical Journal International*, *106*(3), 709-716.

Kisslinger, C., J. R. Bowman, and K. Koch (1981). Procedures for computing focal mechanisms from local (SV/P) z data, *Bull. Seism. Soc. Am.* **71** (6), 1719-1729.

Kwiatek, G., P. Martínez-Garzón, and M. Bohnhoff (2016). HybridMT: A MATLAB Software Package for Seismic Moment Tensor Inversion and Refinement. Seismol. Res. Lett.

Kwiatek, G. and Y. Ben-Zion (2016). Theoretical limits on detection and analysis of small earthquakes. Journal of Geophysical Research-Solid Earth 121, doi 10.1002/2016JB012908

Kwiatek, G. and Y. Ben-Zion (2020). Detection Limits and Near-Field Ground Motions of Fast and Slow Earthquakes. Journal of Geophysical Research: Solid Earth 125, e2019JB018935, doi 10.1029/2019JB018935

Matrullo E., R. De Matteis, C. Satriano, O. Amoroso, and A. Zollo (2013). An improved 1D seismic velocity model for seismological studies in the Campania-Lucania region (Southern Italy), *Geophys. J. Int.* **195**, Issue 1, pp.460-473, doi: 10.1093/gji/ggt224.

Michele, M., S. Custódio, and A. Emolo (2014). Moment tensor resolution: case study of the Irpinia Seismic Network, Southern Italy, *Bull. Seismol. Soc. Am.* **104**, 1348-1357, doi: 10.1785/0120130177.

Pantosti, D., & Valensise, G. (1990). Faulting mechanism and complexity of the November 23, 1980, Campania-Lucania earthquake, inferred from surface observations. *Journal of Geophysical Research: Solid Earth*, *95*(B10), 15319-15341.

Pasquale, G., De Matteis, R., Romeo, A., & Maresca, R. (2009). Earthquake focal mechanisms and stress inversion in the Irpinia Region (southern Italy). *Journal of seismology*, *13*(1), 107-124.

Reasenberg, P., & Oppenheimer, D. USGS (1985). FPFIT, FPPLOT, and FPPAGE: Fortran computer programs for calculating and displaying earthquake fault-plane solutions. *US Geol. Surv. Open-File Rept. 85, 739*.

Satriano, C., Elia, L., Martino, C., Lancieri, M., Zollo, A., & Iannaccone, G. (2011). PRESTo, the earthquake early warning system for southern Italy: Concepts, capabilities and future perspectives. *Soil Dynamics and Earthquake Engineering*, *31*(2), 137-153.

Snoke, J. A., Lee, W. H. K., Kanamori, H., Jennings, P. C., & Kisslinger, C. (2003). FOCMEC: Focal mechanism determinations. *International handbook of earthquake and engineering seismology*, *85*, 1629-1630.

Stabile, T. A., Satriano, C., Orefice, A., Festa, G., & Zollo, A. (2012). Anatomy of a microearthquake sequence on an active normal fault. *Scientific reports*, *2*(1), 1-7.

Steinberg, D. M., Rabinowitz, N., Shimshoni, Y., & Mizrachi, D. (1995). Configuring a seismographic network for optimal monitoring of fault lines and multiple sources. *Bulletin of the seismological society of America*, *85*(6), 1847-1857.

Sokos, E., & Zahradník, J. (2013). Evaluating centroid-moment-tensor uncertainty in the new version of ISOLA software. *Seismological Research Letters*, *84*(4), 656-665.

Tape, W., & Tape, C. (2012). A geometric setting for moment tensors. *Geophysical Journal International*, *190*(1), 476-498.

Tarantino, S., Colombelli, S., Emolo, A., & Zollo, A. (2019). Quick determination of the earthquake focal mechanism from the azimuthal variation of the initial P-wave amplitude. *Seismological Research Letters*, *90*(4), 1642-1649.

Trnkoczy, A., Bormann, P., Hanka, W., Holcomb, L. G., & Nigbor, R. L. (2009). Site selection, preparation and installation of seismic stations. In *New Manual of Seismological Observatory Practice (NMSOP)* (pp. 1-108). Deutsches GeoForschungsZentrum GFZ.

Vavrycuk, V., P. Adamova, J. Doubravová, and H. Jakoubková (2017). Moment Tensor Inversion Based on the Principal Component Analysis of Waveforms: Method and Application to Microearthquakes in West Bohemia, Czech Republic. Seismological Research Letters 88, 1303–1315, doi 10.1785/0220170027

Weber, E., Iannaccone, G., Zollo, A., Bobbio, A., Cantore, L., Corciulo, M., ... & Satriano, C. (2007). Development and testing of an advanced monitoring infrastructure (ISNet) for seismic early-warning applications in the Campania region of southern Italy. In *Earthquake early warning systems* (pp. 325-341). Springer, Berlin, Heidelberg.

Zollo, A., & Bernard, P. (1991). Fault mechanisms from near-source data: joint inversion of S polarizations and P polarities. *Geophysical Journal International*, *104*(3), 441-451.

635 TABLES

636

637

Depth 5 km	Max Distance (km)	No. P-polarities
M_L 1.0 -1.5	30	1
M_L 1.5 - 2.0	49	1
M_L 2.0 - 2.5	57	4
Depth 10 km	Max Distance (km)	No. P-polarities
M_L 1.0 -1.5	33	1
M_L 1.5 - 2.0	40	5
M_L 2.0 - 2.5	66	6

Table 1 Maximum distance of the farthest triggered seismic station and number of P-wave polarities as function of earthquake magnitude and depth. The values, empirically derived from the ISNet bulletin, are used for the earthquake simulations.

682

683

Figure No.	Map	Focal Mechanism Solution	Magnitude Bin	Depth	Noise Level	Dataset
4	Kagan angle misfit	FM1, FM2, FM3	M3	10 km	5%	D1
5	Kagan angle misfit	FM1	M1, M2, M3	10 km	5%	D2, D3
6	focal mechanism parameter misfit	FM1	M1, M2, M3	10 km	5%	D3
7	Kagan angle average	FM1	M1, M2, M3	10 km	5%	D2, D3
8	Kagan angle standard deviation	FM1	M1, M2, M3	10 km	5%	D2, D3
9	focal mechanism error	FM1	M1, M2, M3	10 km	5%	D3
10	Kagan angle misfit	FM1, FM2, FM3	M1, M2, M3	10 km	5%	D3
11	focal mechanism parameter misfit	FM1	M1, M2, M3	5 km	5%	D3
12	Kagan angle misfit	FM1	M1, M2, M3	10 km	30%	D3

684

685 **Table 2.** Summary of the Figures 4-12 with parameters used for earthquake simulations whose results
686 are represented as a specific map.

687

688

689

690

691

692

693

694

695

696

697

698

699

700

701

702

703

704

705

706

707

P-plunge (°)	P-trend (°)	T-plunge (°)	T-trend (°)	Strike (°)	Dip (°)	Rake (°)	Quality
55	344	31	196	325	20	-40	A
51	334	36	181	320	15	-30	A
55	14	31	226	355	20	-40	A
53	205	34	49	180	15	-40	A
55	72	33	272	35	15	-50	A
51	177	32	37	290	80	-110	A
54	292	34	91	10	80	-80	A
77	146	9	7	270	55	-100	B
80	235	10	55	325	55	-90	B
76	103	2	6	110	45	-70	B
76	117	2	214	290	45	-110	B
76	82	7	199	275	40	-110	B
75	190	15	10	280	60	-90	B
75	205	15	25	295	60	-90	B
85	230	5	50	140	40	-90	B
83	146	0	53	150	45	-80	B
80	240	10	60	330	55	-90	B
81	233	5	353	270	50	-80	B
81	347	5	227	130	50	-100	B
55	93	10	198	255	45	-140	C
55	133	10	238	295	45	-140	C
48	130	2	38	275	60	-140	C
48	305	2	37	340	60	-40	C
55	202	7	102	345	60	-130	C
58	121	2	27	270	55	-130	C
58	131	2	37	280	55	-130	C
55	342	7	242	125	60	-130	C
47	138	11	36	165	50	-30	C
49	182	14	289	340	45	-150	C
58	151	2	57	300	55	-130	C
49	168	14	61	190	45	-30	C
59	308	15	64	355	65	-60	C
57	306	14	59	115	40	-140	C
57	76	14	189	245	40	-140	C
45	85	6	348	225	65	-140	C
55	22	7	282	165	60	-130	C
57	241	14	354	50	40	-140	C
55	98	7	198	135	60	-50	C
51	115	2	22	145	55	-40	C
55	147	7	47	290	60	-130	C

Table 3. Fault plane solutions of instrumental seismicity occurred in Irpinia region in 2005-2008 and calculated by De Matteis et al., (2012). The solutions are classified according to a quality code based on the resolution of fault plane kinematics as derived in this study. The result of our simulations suggests a quality as follows: FM1=C, FM2=B, FM3=A.

FIGURES
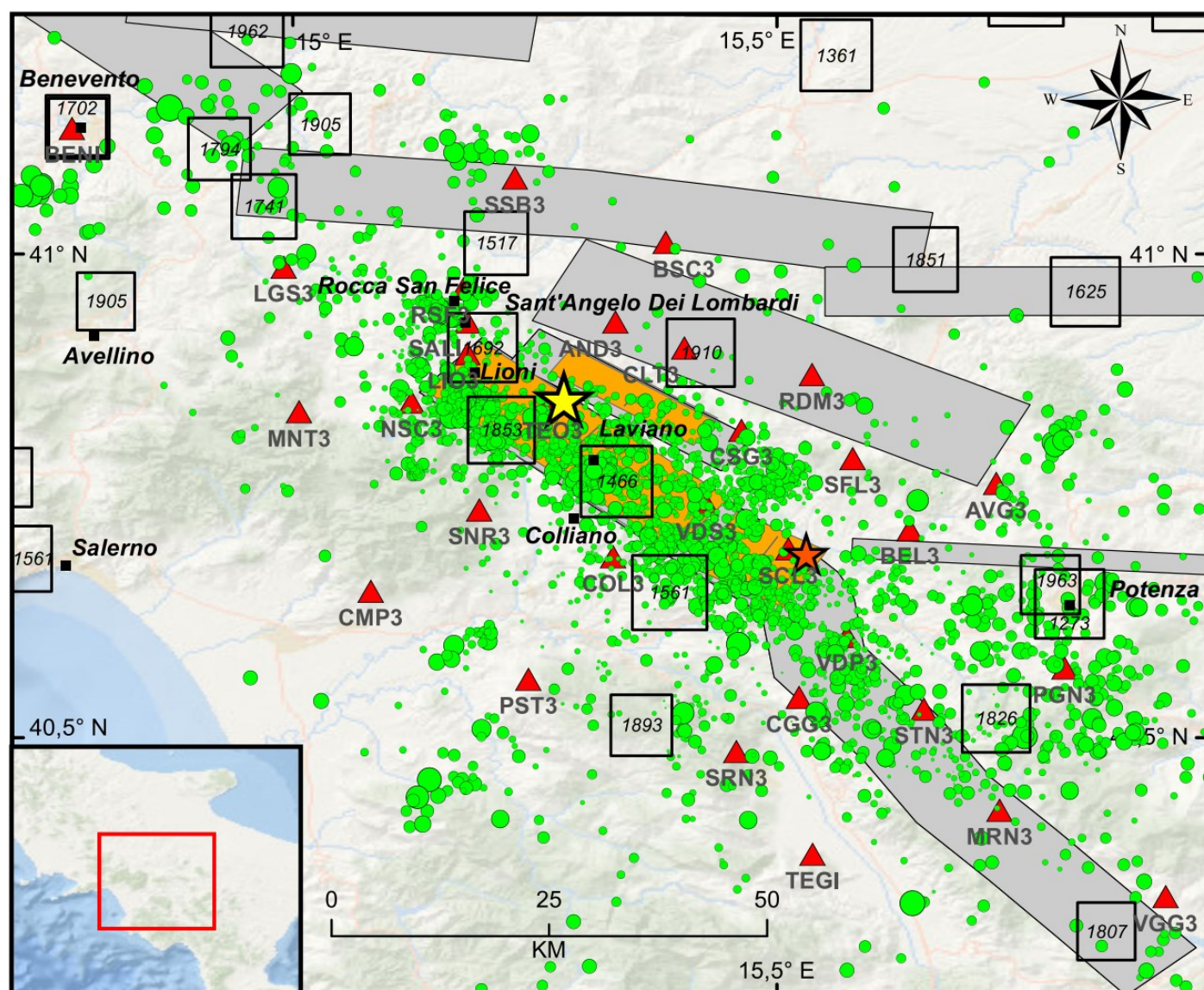
Figure 1. Epicentral map of the earthquakes (green circles) recorded by Irpinia Seismic Network (ISNet, red triangles) from 2008 to 2020 (http://isnet-bulletin.fisica.unina.it/cgi-bin/isnet-events/isnet.cgi). The yellow and orange stars refer to the epicentral location of the 1980, M 6.9, and of the 1996, M 4.9 earthquakes, respectively. Historical seismicity is shown with black squares (I0 ≥ 6–7 MCS). Seismogenic sources related to the Irpinia fault system are indicated by orange rectangles; potential sources for earthquakes larger than M 5.5 in surrounding areas are indicated in grey (Database of Individual Seismogenic Sources, DISS, Version 3.2.1)
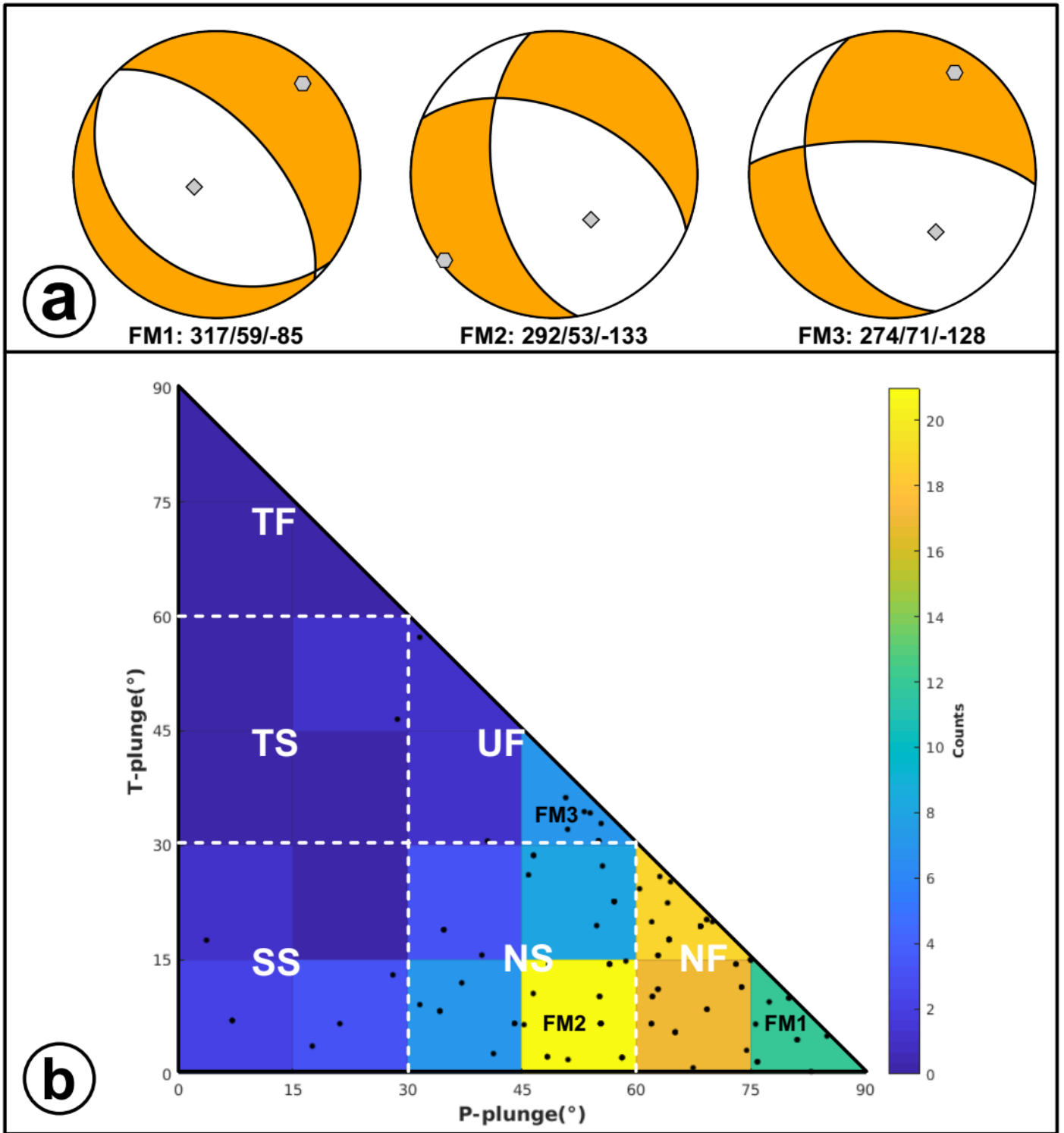
Figure 2. Fault plane solutions used for earthquake simulations. a) From left to right: 1) Ms 6.9, 23rd November 1980 (FM1; Westaway) 2) and 3) Median focal mechanism found from solutions of the 1st (FM2) and 5th (FM3) most populated bin of histogram of panel b. b) Fault plane solutions (black dots) are classified according to the plunge of P- and T-axes with the specific tectonic regimes (Legend: NF, normal fault; NS, normal-strike; SS, strike-slip; TF, thrust ; TS, thrust-strike; UF, unknown fault). The number of earthquakes (colour bar) is counted in bins of 15° × 15°.
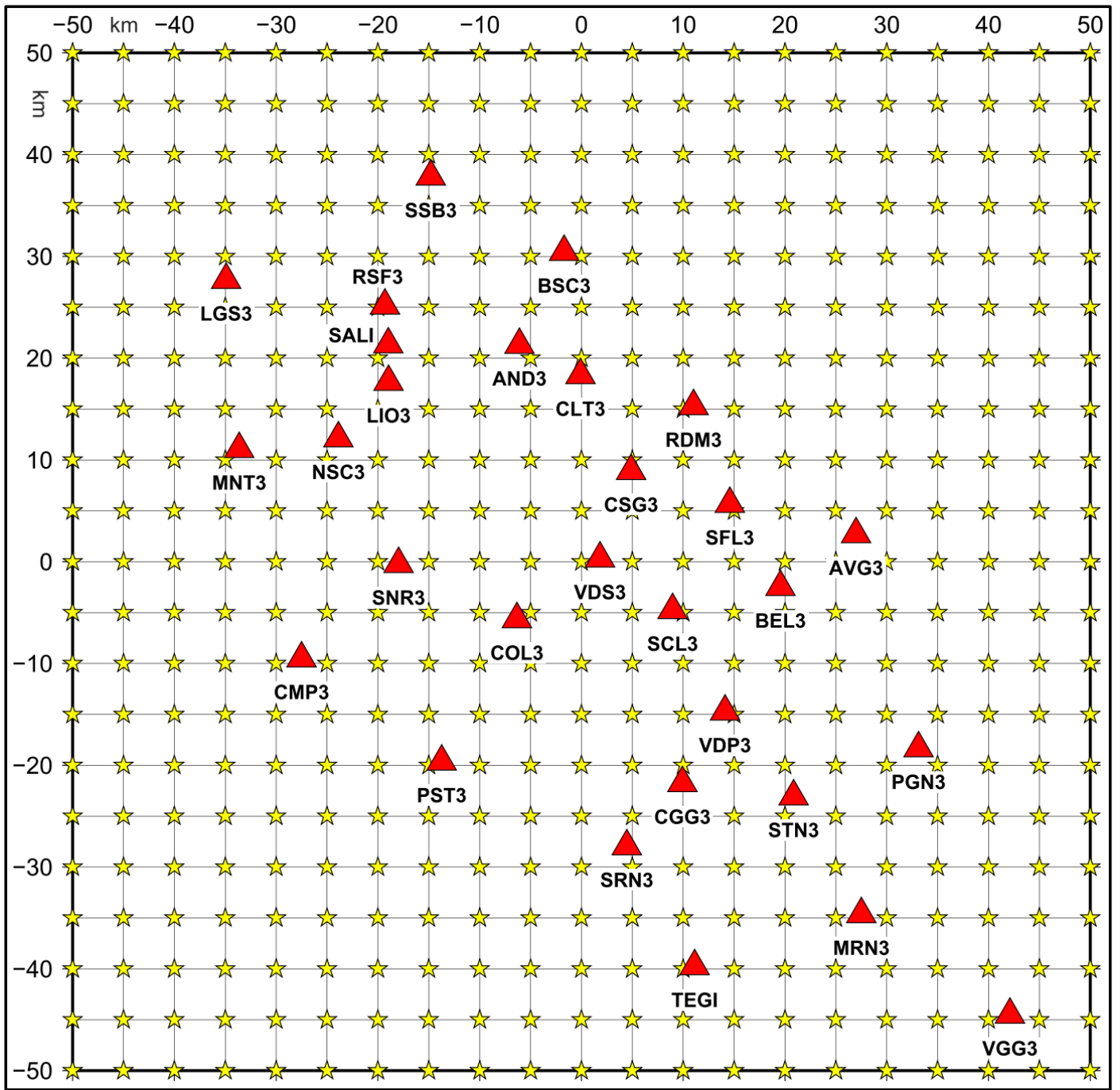
Figure 3. Regular grid of epicentres (yellow stars) used for simulating earthquakes. The area is 100x100 km^2 with 5 km of spacing along both horizontal coordinates. Irpinia Seismic Network (ISNet) is reported with red triangles.
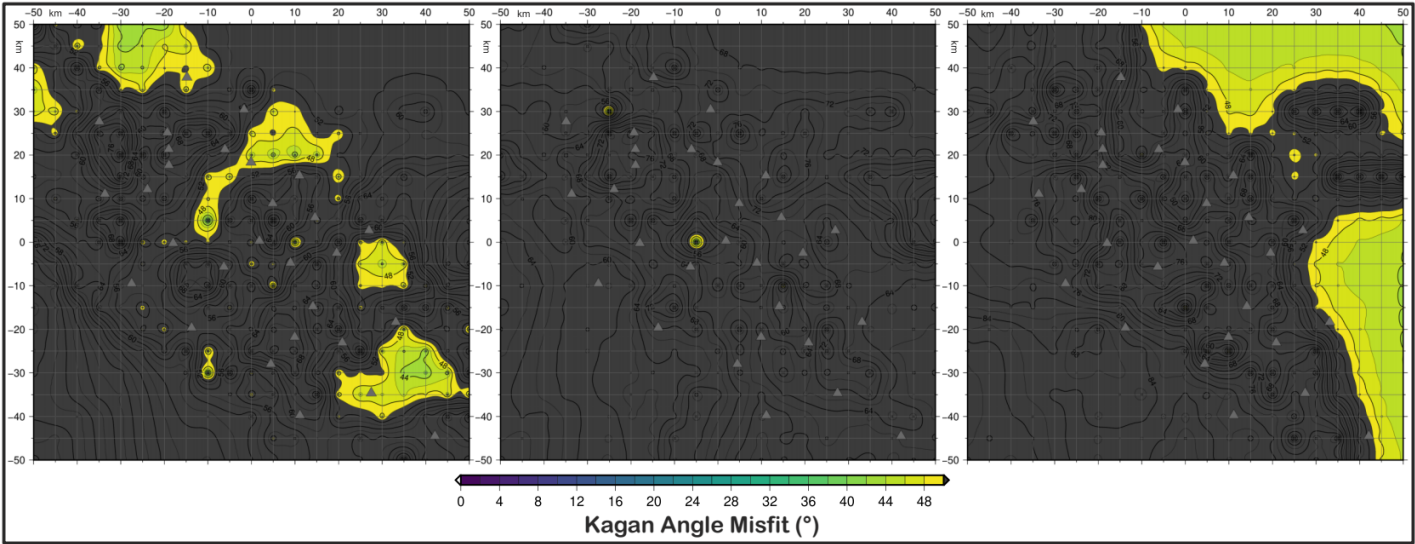
Figure 4. KAM (Kagan angle misfit) map for retrieved focal mechanisms with D1 dataset as input data and simulating earthquakes with M3 magnitude and FM1 (a), FM2 (b) and FM3 (c) theoretical fault plane solution at 10 km depth.
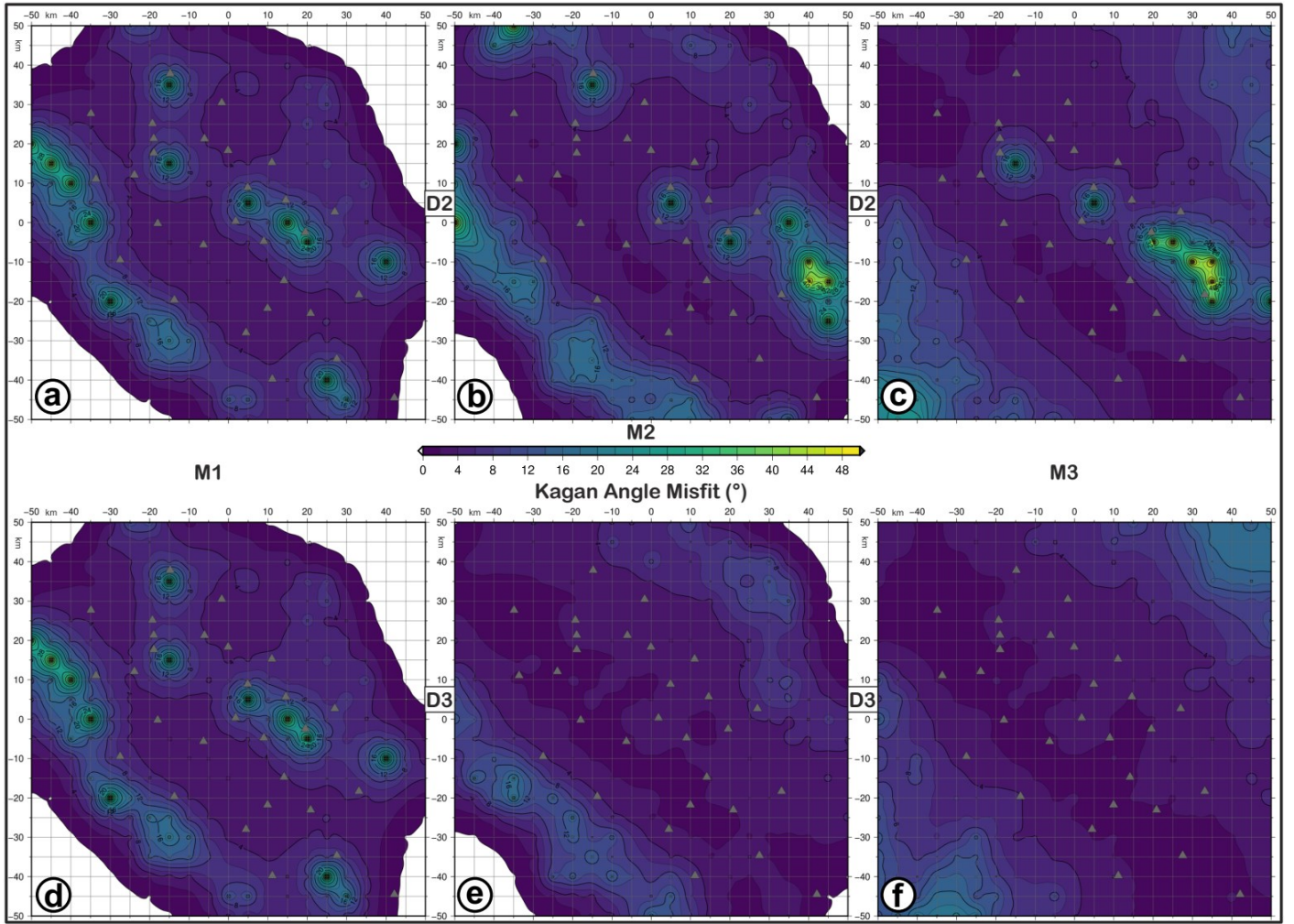
Figure 5. KAM (Kagan angle misfit) map for retrieved focal mechanisms with D2 (a, b, c) and D3 (d, e, f) datasets as input data and simulating earthquakes with M1 (a, d), M2 (b, e) and M3 (c, f) magnitudes and FM1 theoretical fault plane solution at 10 km depth. The level of Gaussian noise is set to 5%.
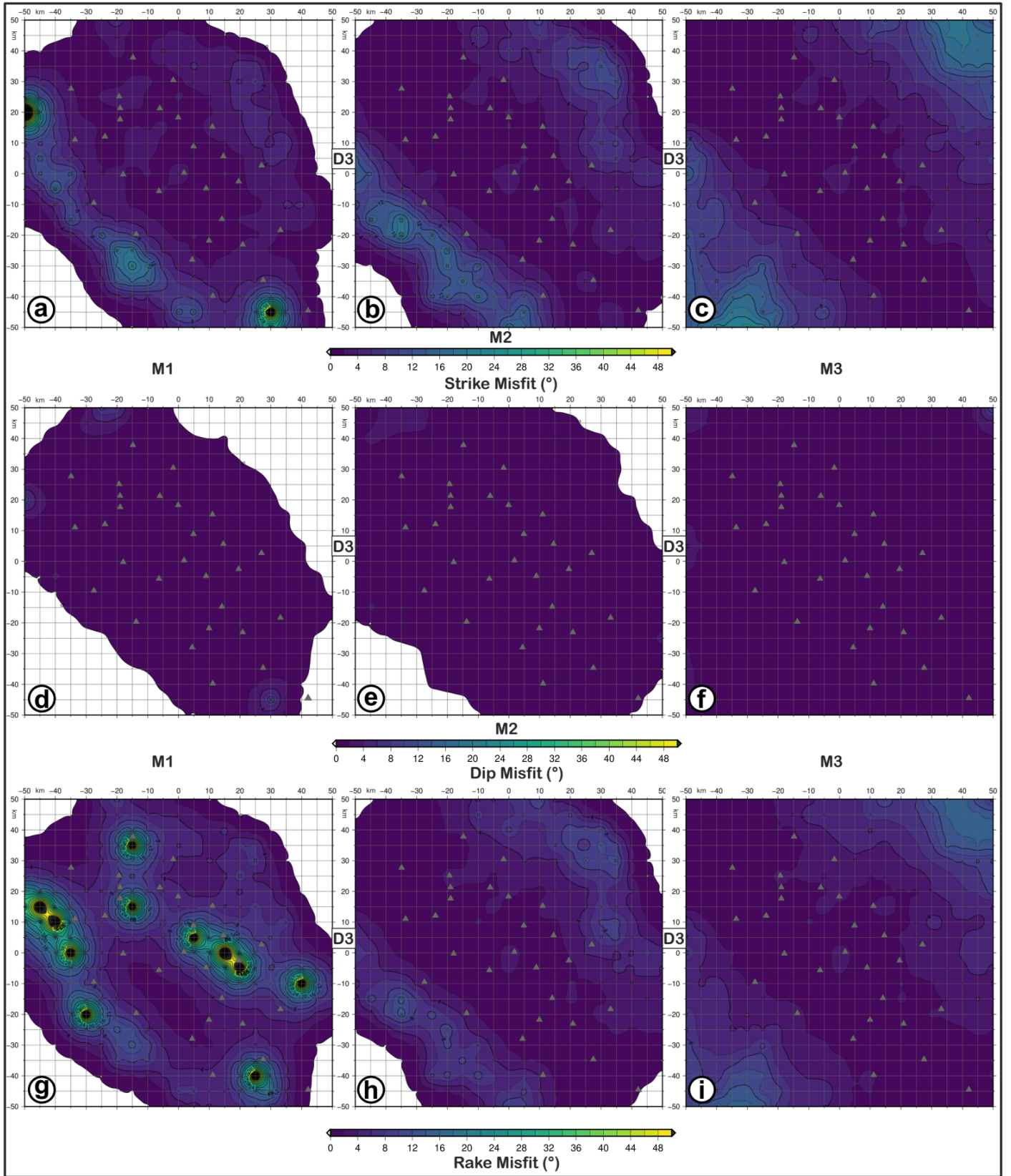
Figure 6. FMM (focal mechanism parameter misfit) maps for retrieved focal mechanisms with D3 datasets as input data and simulating earthquakes with M1 (a, d, g), M2 (b, e, h) and M3 (c, f, i) magnitudes and FM1 theoretical fault plane solution at 10 km depth. a, b, c refer to strike misfit; d, e, f refer to dip misfit; g, h, i refer to rake. The level of Gaussian noise is set to 5%.
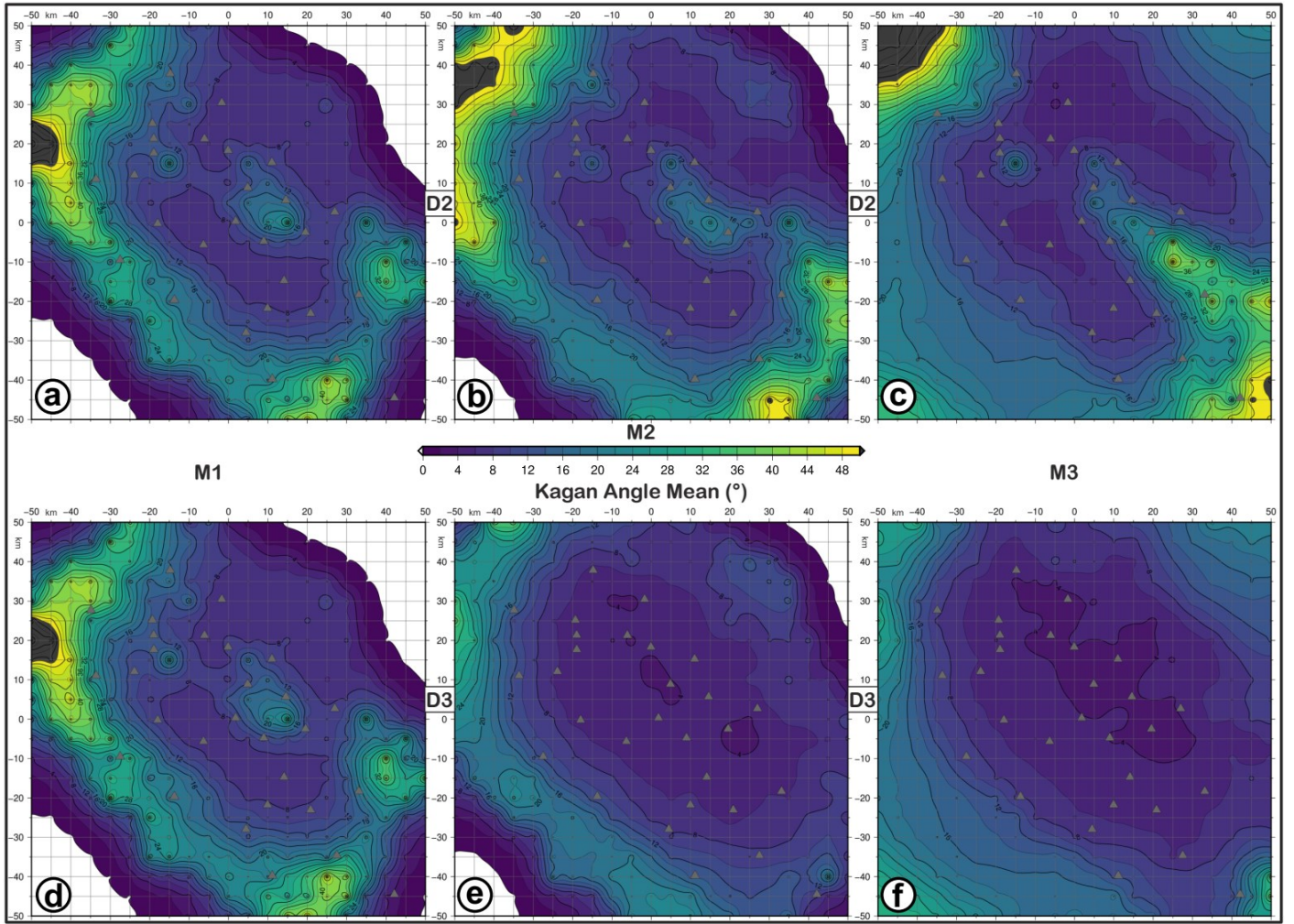
Figure 7. KAA (Kagan angle average) maps for retrieved focal mechanisms with D2 (a, b, c) and D3 (d, e, f) datasets as input data and simulating earthquakes with M1 (a, d), M2 (b, e) and M3 (c, f) magnitudes and FM1 theoretical fault plane solution at 10 km depth. The level of Gaussian noise is set to 5%.
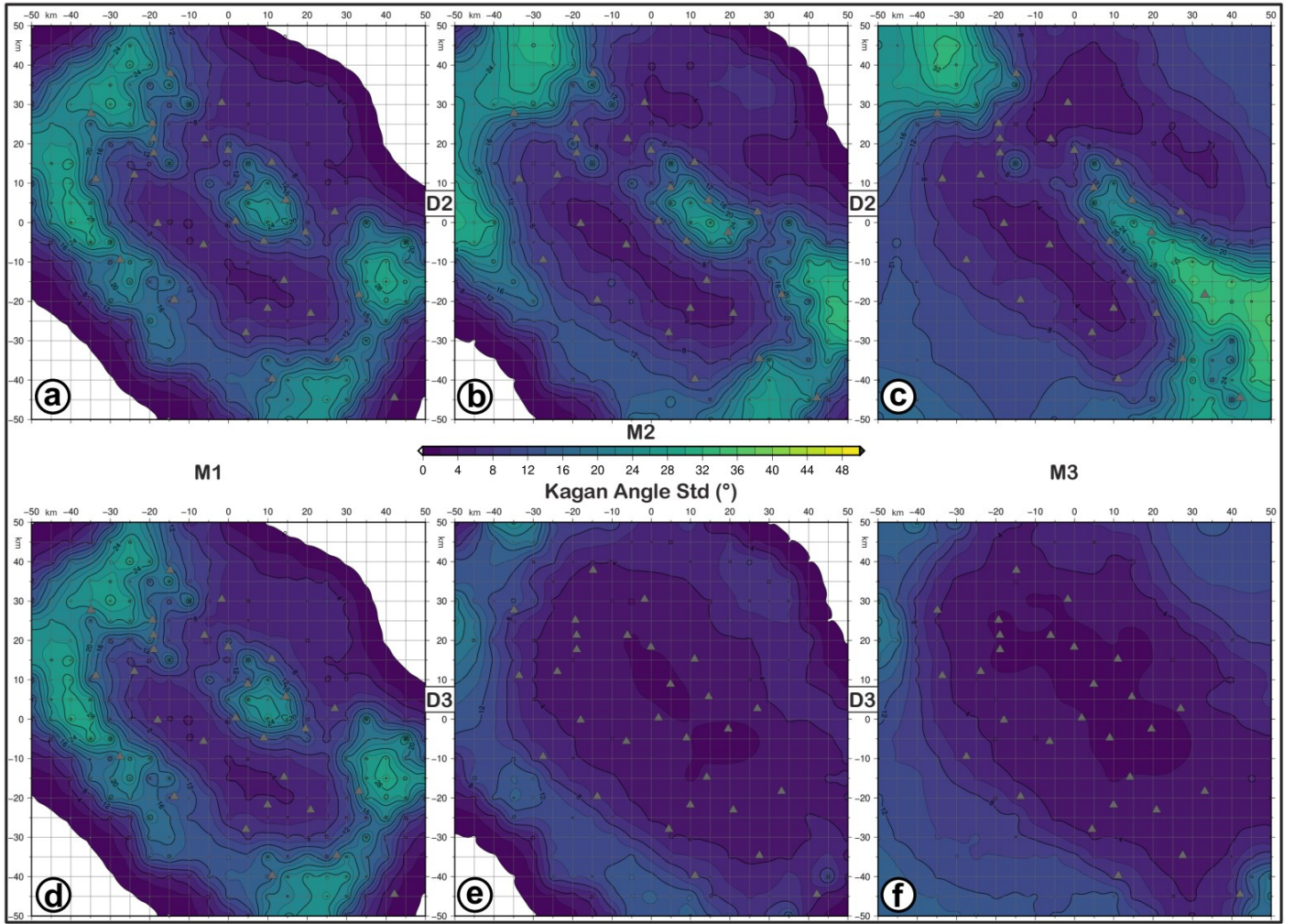
Figure 8. KAS (Kagan angle standard deviation) maps for retrieved focal mechanisms with D2 (a, b, c) and D3 (d, e, f) datasets as input data and simulating earthquakes with M1 (a, d), M2 (b, e) and M3 (c, f) magnitudes and FM1 theoretical fault plane solution at 10 km depth. The level of Gaussian noise is set to 5%.
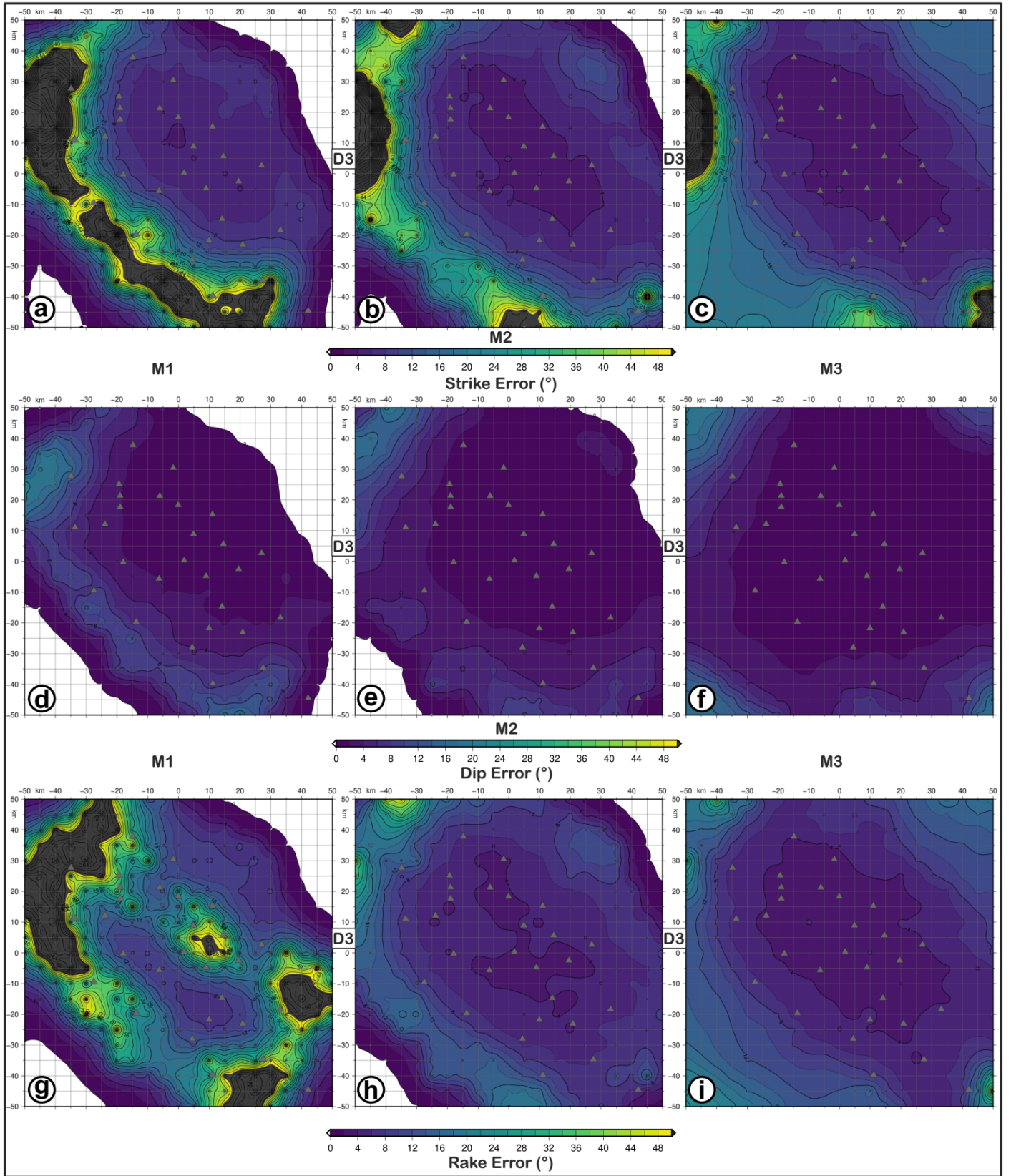
Figure 9. FME (strike, dip and rake error) maps for retrieved focal mechanisms with D3 datasets as input data and simulating earthquakes with M1 (a, d, g), M2 (b, e, h) and M3 (c, f, i) magnitudes and FM1 theoretical fault plane solution at 10 km depth. a, b, c refer to strike error; d, e, f refer to dip error; g, h, i refer to rake error. The level of Gaussian noise is set to 5%.
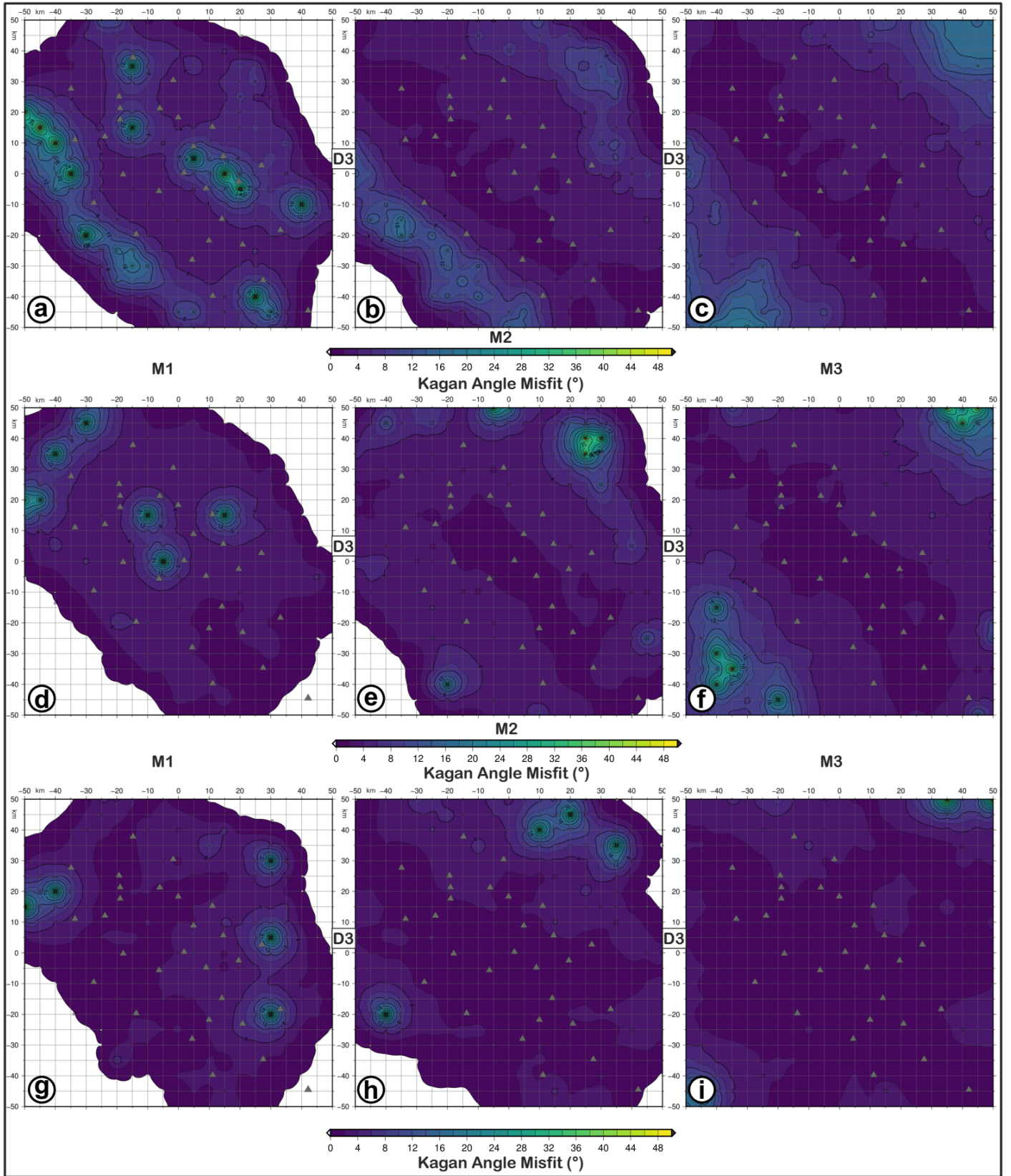
Figure 10. KAM (Kagan angle misfit) maps for retrieved focal mechanisms with D3 datasets as input data and simulating earthquakes with M1 (a, d, g), M2 (b, e, h) and M3 (c, f, i) magnitudes and FM1 (a, b, c), FM2 (d, e, f) and   FM3 (g, h, i) theoretical fault plane solution at 10 km depth. The level of Gaussian noise is set to 5%.
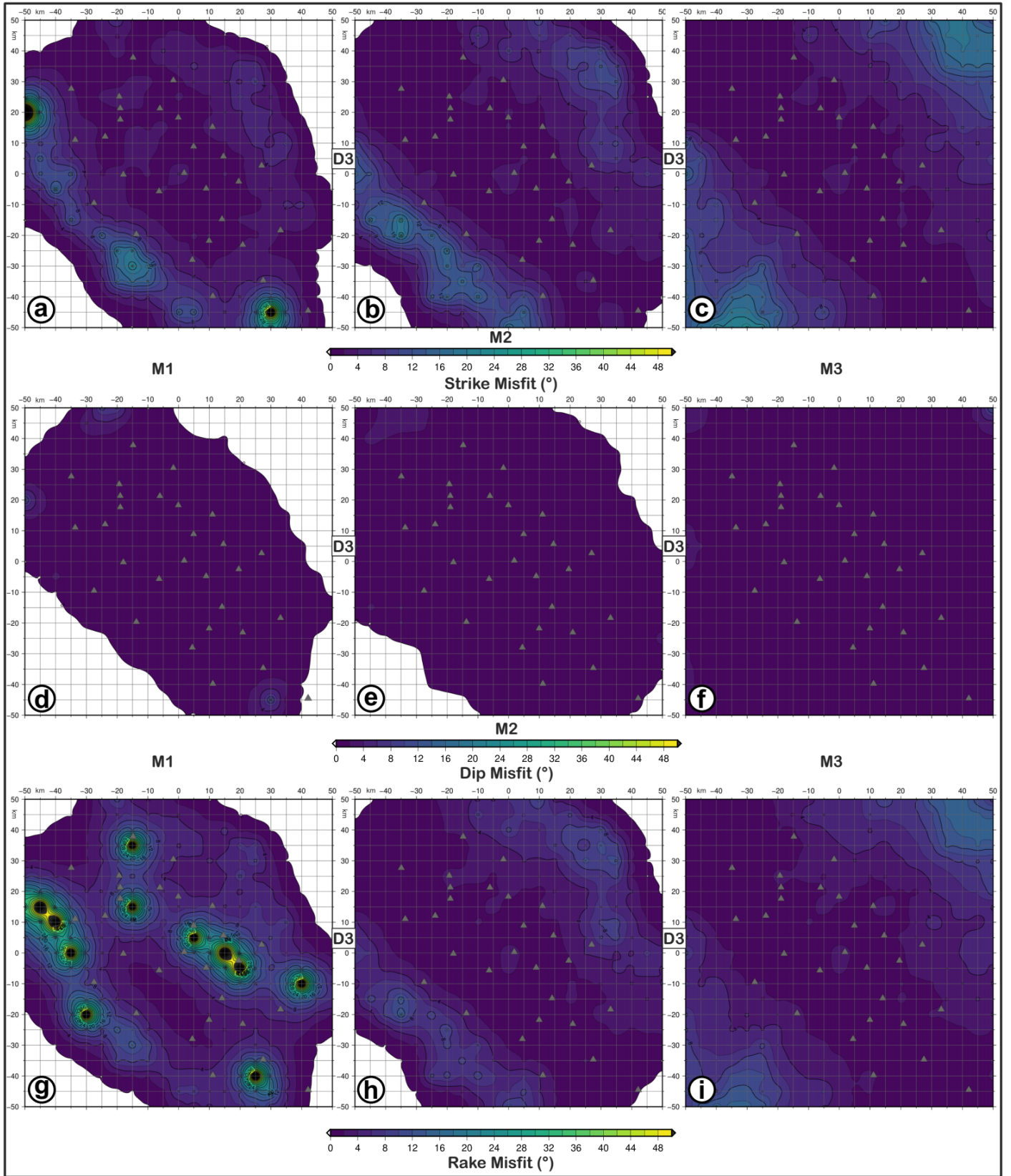
Figure 11. FMM (focal mechanism parameter misfit) maps for retrieved focal mechanisms with D3 datasets as input data and simulating earthquakes with M1 (a, d, g), M2 (b, e, h) and M3 (c, f, i) magnitudes and FM1 theoretical fault plane solution at 5 km depth. a, b, c refer to strike misfit; d, e, f refer to dip misfit; g, h, i refer to rake. The level of Gaussian noise is set to 5%.

864
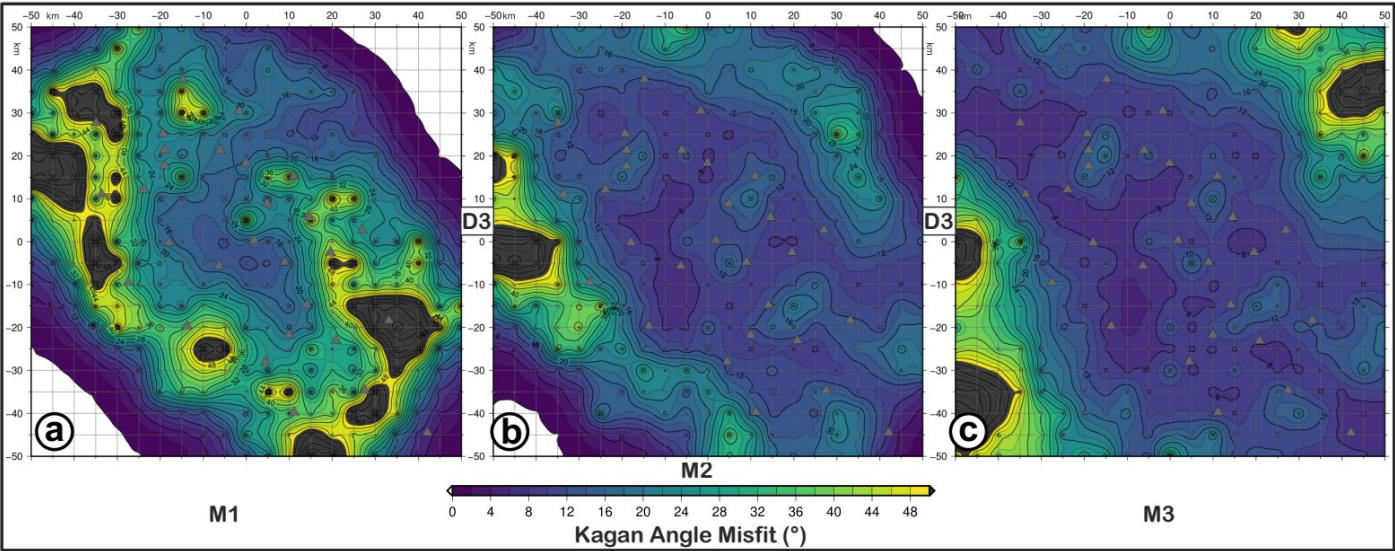
865
866
867 **Figure 12.** KAM (Kagan angle misfit) map for retrieved focal mechanisms with D3 (a, b, c) datasets as
868 input data and simulating earthquakes with M1 (a), M2 (b) and M3 (c) magnitudes and FM1 theoretical
869 fault plane solution at 10 km depth. The level of Gaussian noise is set to 30%.
870
871
872
873
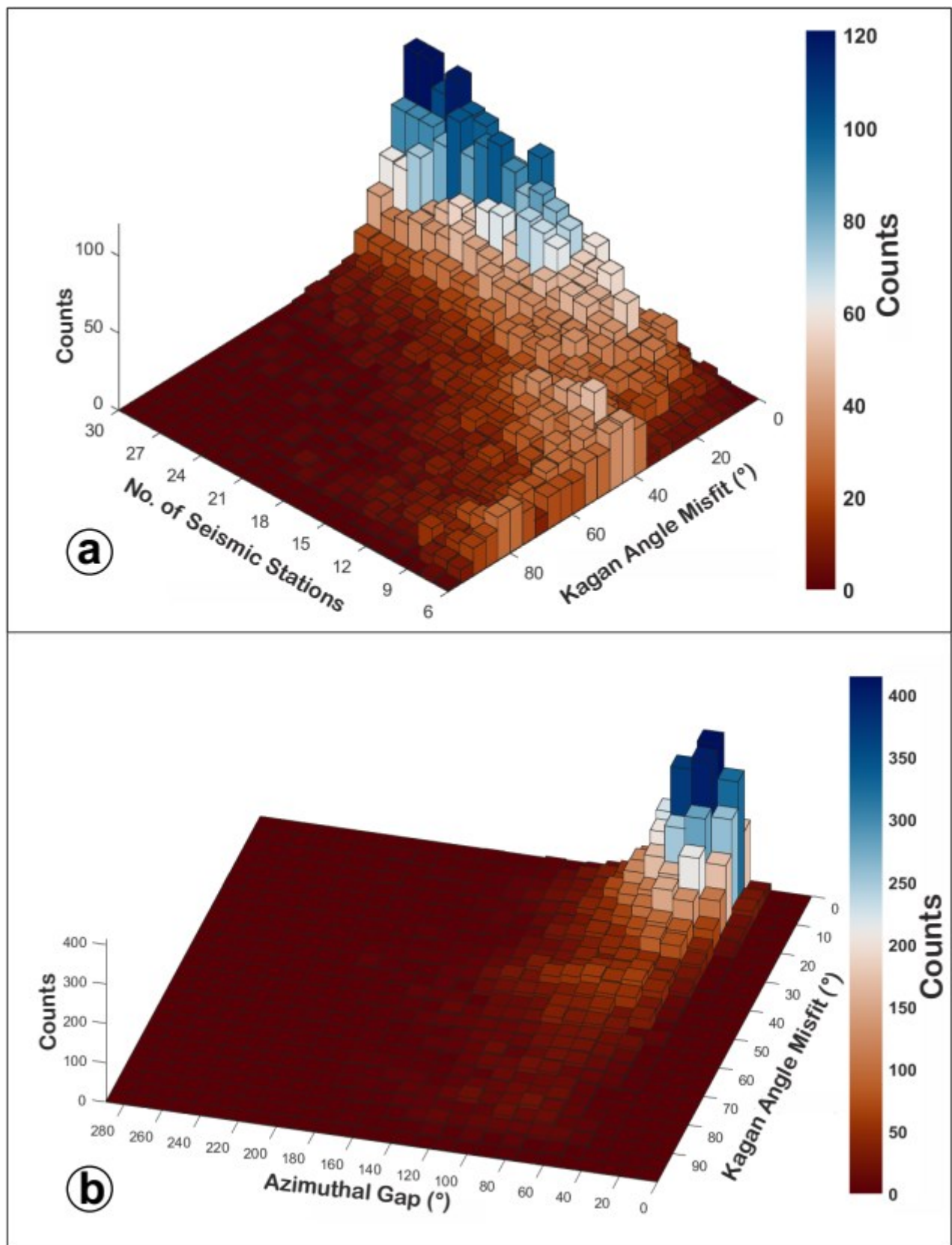
Figure 13. 3D-histograms of the test results in terms of number of stations (a), azimuthal gap (b) and KA misfit. The simulations were carried out with a free network configuration.